Journal of Applied Physics

RESEARCH ARTICLE | FEBRUARY 26 2025

Spatial description of dislocation nucleation in the shock response of single-crystal aluminum

Andre Archer ; Kaitlyn Campbell ; Douglas E. Spearot

J. Appl. Phys. 137, 085102 (2025)
https://doi.org/10.1063/5.0239019

Journal of Applied Physics ARTICLE pubs.aip.org/aip/jap

Spatial description of dislocation nucleation in the shock response of single-crystal aluminum

Cite as: J. Appl. Phys. **137**, 085102 (2025); doi: 10.1063/5.0239019
Submitted: 16 September 2024 · Accepted: 2 February 2025 ·
Published Online: 26 February 2025

View Online Export Citation CrossMark

Andre Archer,[1] Kaitlyn Campbell,[1] and Douglas E. Spearot[1,2,a)]

AFFILIATIONS

[1]Department of Mechanical and Aerospace Engineering, University of Florida, Gainesville, Florida 32611, USA
[2]Department of Materials Science and Engineering, University of Florida, Gainesville, Florida 32611, USA

[a)]**Author to whom correspondence should be addressed:** dspearot@ufl.edu. **Tel.:** 352-392-6747.

ABSTRACT

Nonequilibrium molecular dynamics simulations of shock loaded single-crystal Al in the ⟨100⟩, ⟨110⟩, ⟨111⟩, and ⟨123⟩ orientations are conducted to study elastic and plastic shockwave formation and details associated with dislocation activity. A computer vision-based approach is implemented to capture the presence of dislocations and describe their spatial characteristics in the zone of nucleation behind the propagating shockwave. The methodology developed relies on the sequences of images extracted during shock loading that show dislocation activity within a cross section of the sample. Results reveal that the spacing between activated slip systems is orientation dependent and exhibits a modest reduction for the ⟨100⟩ and ⟨111⟩ orientations as shock pressure increases. Comparisons are made to existing theoretical models. Such relationships between shock pressure and dislocation activity, extracted from molecular dynamics simulations, can be used to inform higher length scale simulations or modeling of dislocation-based plasticity during shock.

I. INTRODUCTION

A key challenge in developing materials for extreme environments is being able to analyze and understand deformation mechanisms during events such as shock. This extreme thermomechanical loading state is common during impacts from micrometeorites, materials subjected to explosives, or laser–material interactions.[1] The response of metallic materials subjected to strong shocks, during which they undergo instantaneous melting or amorphization, is relatively well documented.[1–4] Less understood is the response of metallic materials just at or above the Hugoniot elastic limit (HEL), the point at which plastic deformation occurs in a material undergoing shock.

For metals, where dislocations are the governing mechanism, the Orowan equation[5] describes the plastic strain, γ, as a function of the density and motion of dislocations,

$$\gamma = k\rho b\bar{l}. \tag{1}$$

Here, ρ is the mobile dislocation density, $\bar{l}$ is the mean distanced traveled by dislocations in the sample, b is the magnitude of the Burgers vector, and k is a material specific constant. To describe the rate of plastic strain, one can take the time derivative of Eq. (1),[6]

$$\dot{\gamma} = kb\left(\rho\frac{d\bar{l}}{dt} + \bar{l}\frac{d\rho}{dt}\right). \tag{2}$$

The first term on the right-hand-side, $\rho\frac{d\bar{l}}{dt}$, describes the rate at which dislocations move through the material. This term dominates during low strain rate loading since most of the plastic strain is due to the motion of pre-existing dislocations. The second term on the right-hand-side, $\bar{l}\frac{d\rho}{dt}$, is necessary for extremely high strain rates. In essence, the pre-existing dislocations in a network may not be able to move fast enough to accommodate the extremely high strain rate imposed on the material; so, this second term accommodates the plastic strain via increasing the dislocation density through nucleation events.

The first attempt to spatially describe shock-induced dislocation nucleation was by Smith in 1958; they proposed an array of geometrically necessary dislocations to relax the lattice between compressed and uncompressed regions, forming a Smith interface.[7] This model was expanded on by Hornborgen to include screw

dislocations left behind the shock front, accounting for the deformed material after the wave has passed.[8] Both of these models considered that dislocations could move with the shock front, which would require them to travel supersonically through the lattice. In the derivation of a model for the dislocation density resulting from a shockwave, Meyers *et al.* proposed a homogenous nucleation mechanism in which the deviatoric components of stress are relaxed by dislocations that are periodically nucleated behind the shock front.[9,10] This was the first model to propose a mechanism for plastic wave motion that does not require dislocations to travel supersonically. Dislocations are nucleated homogeneously as a planar array and then grow into loops.[9] Once the elastic wave has traveled far enough to build up additional deviatoric stresses, a new layer of dislocations is nucleated.[9] Weertman considered both models in the analysis of strong shocks, where a Smith interface is envisioned to exist; but, as the shock pressure increases, the number of dislocations that are mobile must also increase in order to multiply in the elastic–plastic zone.[11,12] More recently, the work by Pellegrini and Josien considered the nucleation of dislocations behind the plastic front as well as the nucleation of dislocations between the elastic and plastic fronts moving supersonically, based on one-dimensional atomistic simulations, and developed a model of dislocation spacing to describe the dislocation densities behind a shock front with the use of a Peierls model for plasticity.[13]

In situ experimental observation of dislocation nucleation during shock is extremely difficult, if not impossible, due to the time and length scales involved. Therefore, computational modeling and simulation methods are necessary to advance and test the previously mentioned models. Using nonequilibrium molecular dynamics (MD) simulations, it is possible to study the atomic structure of a material behind a propagating shockwave, allowing the observation and measurement of dislocation behavior as it dynamically evolves. Dislocation generation in shockwaves can be seen in early MD simulations by Mogilevsky *et al.* in which shear stress relaxation was recorded when holding a sample at the peak shock pressure over time.[14] Holian demonstrated the capability of nonequilibrium MD simulations to characterize the Hugoniot states of shock and proposed MD as a way to investigate plasticity.[15] Since then, the use of MD simulations to analyze shock phenomena has grown extensively with larger, more representative models enabled by increasing computational power and more accurate interatomic potentials.

The MD simulations of shockwave propagation have been performed extensively on both single crystal and polycrystalline metals, especially Al and Cu, with significant work performed to characterize the Hugoniot states of materials with applications that include explorations of elastic anisotropy, spallation, and the effect of pores at high shock pressures.[3,16–29] The Rankine–Hugoniot behavior of metals under strong shocks is commonly studied and reveals a linear equation of state (EOS) between shockwave speed and piston speed,[16]

$$u_s = \lambda u_p + c_0. \tag{3}$$

The relationship between the piston velocity, u_p, and the shockwave velocity, u_s, is linearly proportional to λ , and constant c_0 is the longitudinal speed of sound. At very high piston velocities, the plastic front is overdriven, and the relationship presented in Eq. (3) is accurate as a linear fit since the plastic wave travels with the elastic front. As the piston speed decreases, the plastic wave speed slows down while the elastic wave speed plateaus. This trend continues until the piston velocity is lower than the HEL, where no plastic response occurs. Shock velocities just at or above the Hugoniot elastic limit will be the primary subject of this study since this is where the shock response is predominantly the result of dislocation nucleation and motion.

Several prior studies have qualitatively characterized the dislocation network generated by a shockwave. For example, experiments showed that when Al or Cu undergo a loading below the shock-melting point, the dislocation network generated consists of a structure of stacking faults that form crosshatched cells aligned with the {111} slip planes for FCC metals,[6] with the specific activated slip systems being a result of the crystallographic direction of shock loading. In MD simulations, this same pattern of stacking faults has been observed through common-neighbor analysis, indicating the presence of Shockley partial dislocations and their connecting stacking faults.[12,15–20] Activated slip systems during loading are dependent on the lattice orientation relative to the direction of loading, implying the development of these stacking faults and their spatial organization is orientation dependent. Therefore, it is necessary to consider the orientation dependence of the Hugoniot and other associated properties when characterizing dislocation nucleation and growth.

Nonequilibrium MD simulations by Xu *et al.* on single-crystal Cu with shock oriented along ⟨001⟩, ⟨111⟩, and ⟨110⟩ showed anisotropy in the plastic wave speed for each shock direction, which is explained through consideration of Schmid factors for each orientation.[30] However, the primary takeaway from their work was the identification of different regimes of the plastic wave speed. Xu *et al.* described regions in which the plastic wave speed was dominated by the growth of the existing dislocations as well as a shock regime in which the plastic wave speed required dislocation nucleation and growth together. The plastic wave speed was considered to be entirely dominated by the nucleation events once the plastic wave is overdriven and is traveling with the elastic wave front.[30] They were able to capture the events in which embryos of dislocations were formed ahead of the plastic wave front, causing the instantaneous velocity of the plastic wave to be much faster than the elastic wave speed. Dislocation embryo formation also caused local disruptions in the stress state that could be quantified by bands in the x–t diagrams.[30] However, the spatial characteristics of dislocations in separate regimes were not described with respect to shock pressure and their discussion was limited to the ⟨110⟩ orientation. A similar phenomenon was reported by Zhakhovsky *et al.*[31] using a moving-window MD method to shock ⟨111⟩ Al samples where ultrashort elastic pulses were emitted by dislocations in the plastic front that travel toward the elastic front at the local sound speed. According to Zhakhovsky *et al.*, when these pulses catch up to the elastic front, the speed of the elastic and plastic fronts become synchronized, resulting in a regular spacing between the elastic and plastic fronts on the order of hundreds of nanometers.[31] Similar to Xu *et al.*, the fluctuations in the elastic stresses were traced to the generation of dislocations that then multiply rapidly to relax the local stress state in the plastic region.[30,31]

In this work, the shock response of Al single crystals is analyzed using nonequilibrium molecular dynamics simulations. The key novelty is that the development and spatial arrangement of dislocations immediately behind the shock front is quantified using a machine vision approach. Specifically, spatial descriptions of dislocation nucleation are obtained through the image analysis of multiple sampled and rendered images of the regions behind the shock front where dislocations nucleate, leveraging the patterns of stacking faults that identify the activated slip planes to compute an average spacing between nucleated dislocations. An important note for this work is that the results presented and discussion around dislocations refer almost exclusively to Shockley partial dislocations that include stacking faults. While other types of dislocations and defects exist in aluminum during shock, most of them are of Shockley type and are utilized as the objects to be detected through machine vision.

It is shown that as the shock pressure increases, the spacing between adjacent dislocations at the shock front decreases up to the point where shock-induced melting begins. In line with the homogenous dislocation nucleation model by Meyers,[6,9] length scales are extracted that align with the elastic–plastic wave separation, h, and the spacing between adjacent dislocations in a homogenously nucleated array, d. Ultimately, a relationship is extracted from MD simulations that quantifies the average dislocation spacing as a function of shock pressure, which then can be used to inform higher length scale simulations or modeling to properly include dislocation nucleation during shock in Al.

II. SIMULATION METHODS

Nonequilibrium MD simulations are performed using the Large-scale Atomic/Molecular Massively Parallel Simulator (LAMMPS) code[32] with an EAM interatomic potential for Al developed by Zhakovskii *et al.*[33] This interatomic potential is chosen due to its ability to accurately capture compressive wave behavior at higher temperatures and short time scales since it was developed based on cold pressure curves to emulate the rapid compression of Al during femtosecond laser ablation.[33] As discussed by Zhakovskii, these EAM potentials capture the highly compressed states of Al better than the potentials from Mishin *et al.*,[34] which are optimized for Al at standard conditions.[33]

Four different sets of simulations are performed on FCC single-crystal Al with various loading directions with respect to the crystal orientation. The loading directions sampled are ⟨100⟩, ⟨111⟩, ⟨110⟩, and ⟨123⟩ to explore slip activity in systems with 8, 6, 4, and 1 active slip systems, respectively, according to the basic Schmid factor analysis. In each simulation, the direction of loading is aligned with the x axis. The simulation cell size is approximately $500 \times 20 \times 20\ \text{nm}^3$ with periodic boundary conditions imposed in the x, y, and z directions, as shown in Fig. 1. The lateral dimensions of the sample are similar to that used by Sharma and Dubey[21] as well as by Germann *et al.*[35] where it is concluded that larger cross sections do not result in significant differences in behavior. This results in between 12 and 12.5×10^6 atoms in each simulation, depending on their lattice orientation. To equilibrate the models, energy minimization is performed first, followed by a Nosé–Hoover style NPT equilibration along to 298 K and 0 bar for 20 ps.

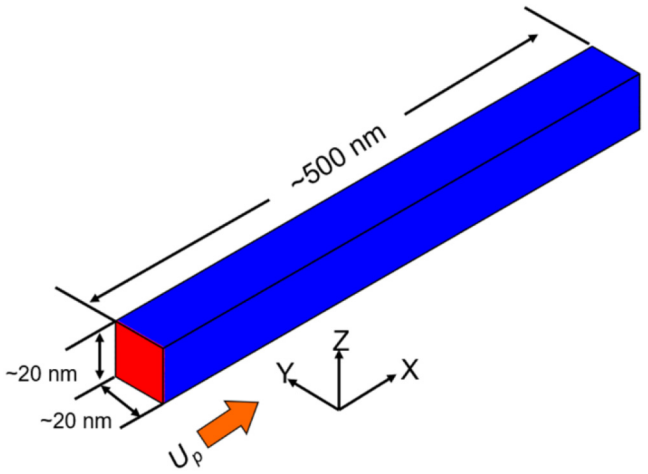

FIG. 1. Single-crystal Al model used for shock simulations measuring approximately $500 \times 20 \times 20\ \text{nm}^3$ with the direction of shock loading oriented along the x axis. Figure dimensions not to scale.

Immediately following equilibration, the periodic boundaries along the x-direction are changed to free surfaces so that shock loading can be applied. The piston ramp is initiated immediately after changing the boundary conditions.

A shockwave is generated through the ramped piston method as described by Wen *et al.*[36] in which a stationary plane of atoms measuring two lattice units thick in the direction of shock acts as a piston and the velocity of the piston is linearly ramped in the x-direction from the rest to its set velocity over 1 ps. Once the piston has reached its desired velocity, it is held at that velocity to sustain the shockwave in the material as the wave travels down the sample. In this study, the wave is allowed to propagate for 50 ps following the ramp period and the simulation is stopped before the elastic wave reaches the end of the sample. This study explores piston velocities from 0.2 to 3.0 km/s, with a higher resolution of piston speed sampled between 0.8 and 1.6 km/s to focus on the regime immediately around the HEL for each crystal orientation.

The stress associated with each atom is calculated by using the per-atom virial stress divided by the per-atom volume obtained from the Voronoi tessellation surrounding each atom.[32] The virial stress for each atom is determined using the y and z components of velocity, removing the x component to negate the effect of the streaming velocity of the sample. While this is not the same as subtracting the streaming velocity for each atom in the shock direction and using all thermal components in the analysis, supplemental calculations were performed to compare the two methods resulting in less than 0.01% difference for shock pressure. One-dimensional spatial binning of the thermomechanical variables is performed within LAMMPS to compute averages, where each bin consists of around 40 000 atoms.

Dislocation activity is identified using centrosymmetry and common-neighbor analysis (CNA), which identify the location of stacking faults based on the local configuration around each

atom.[37–39] Post processing using the Python implementation of OVITO[40] is used to spatially bin the local structure of the sample using one-dimensional bins along the length of the sample and determine the location of the plastic wave, which will be discussed further in the measurement of average dislocation spacing.

III. RESULTS OF SHOCK SIMULATIONS

Visualization of per-atom thermomechanical variables during each shock simulation offers insight into the bulk thermomechanical behavior as the shockwave traverses the sample. As an example, atomic values of centrosymmetry, hydrostatic pressure, and shear stress are presented in Fig. 2 for shock along ⟨111⟩ with a piston velocity of $u_p = 1.3$ km/s. In Fig. 2(a), the development of stacking faults can be seen as the wave travels through the sample from left to right, which indicates the nucleation and growth of dislocations. By aligning this with the per-atom values for hydrostatic and shear stresses, as shown in Figs. 2(b) and 2(c), the elastic–plastic wave separation becomes visible. At the elastic shock front, there is an increase in both hydrostatic and shear stresses with no stacking faults present. Trailing this initial front is the development of stacking faults that align with a secondary jump in hydrostatic stress and a drop in shear stress.

Elastic and plastic wave velocities are obtained from the profiles of shear stress for the ⟨111⟩, ⟨110⟩, and ⟨123⟩ oriented shock samples and are obtained using the hydrostatic stress profile for the ⟨100⟩ orientation. Shear stresses are used for the first three orientations since shock loading along these directions generates an elastic–plastic wave separation that allows the location of the separate fronts to be tracked over time. The initial rise in shear stress is considered as the elastic front while the subsequent drop is identified as the plastic front. Specifically, these points are computed as the positions at which the shear stress reaches 25% of the maximum shear stress, with the leading position identifying the elastic front and the trailing position the plastic front. For ⟨100⟩ shock loading, there is no elastic–plastic wave separation, so the hydrostatic stress must be used to track the elastic front accurately. This orientation uses the same 25% threshold for the computation of the elastic front using the hydrostatic stress.

Calculation of elastic and plastic wave velocities is performed by tracking their positions over 0.1 ps time intervals (100 time steps) and using a second order centered difference method to compute the time derivative. The elastic–plastic separation for each orientation is understood by plotting u_s vs u_p in Fig. 3. The plastic wave velocity, u_s^{plastic}, indicated by the closed symbols, is less than the elastic wave speed, u_s^{elastic}, represented by the open symbols, up until the point where the shockwave is overdriven and there is no elastic–plastic wave differentiation. At this point and above, the shockwave velocity u_s follows the linear equation of state from Eq. (3). For ⟨100⟩ oriented shock, the first sign of dislocation activity is at a shock pressure of 0.9 km/s. For the other orientations, the piston velocity corresponding to the HEL is identified by a "kink" in the plot of pressure vs piston velocity. Aside from the deviation in the initial onset of dislocation activity, which is expected from a Schmid analysis of each loading orientation, the remainder of the Hugoniot curve for each sample is very similar within the shock pressures sampled.

In Fig. 3(a), the ⟨100⟩, ⟨123⟩, and ⟨110⟩ oriented samples all show dislocation activity at a piston velocity of 0.9 km/s, while the

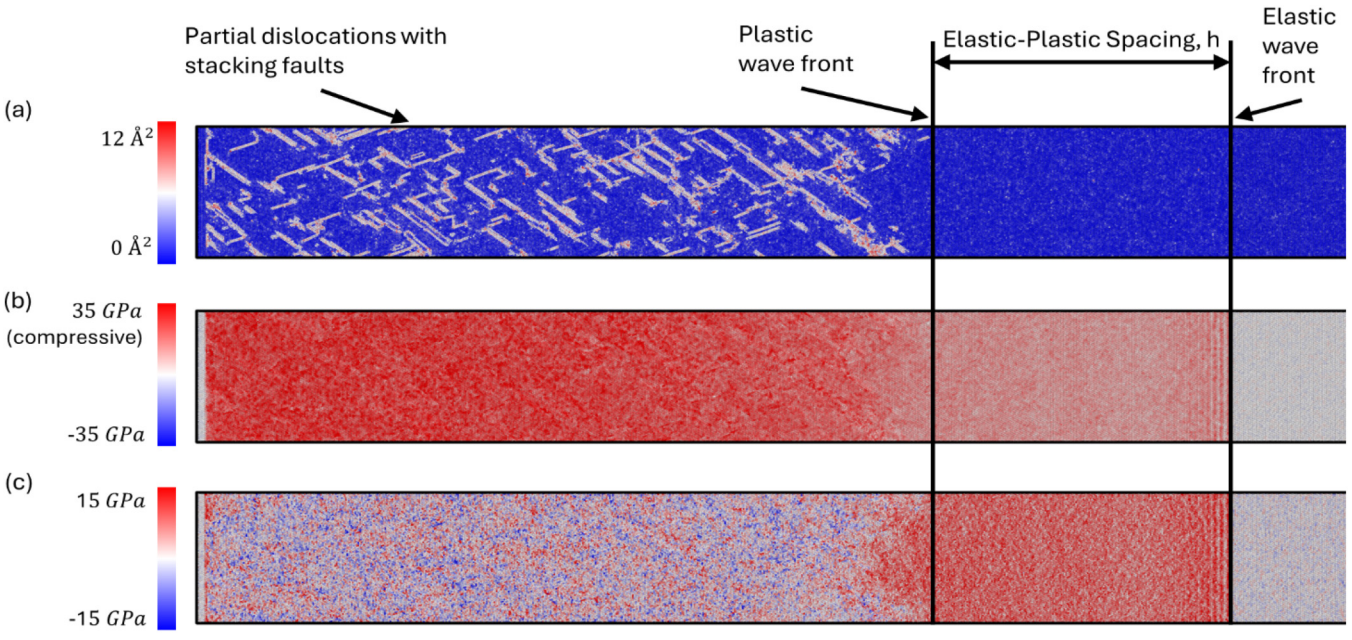

FIG. 2. Example of the MD simulation results with $u_p = 1.3$ km/s oriented along ⟨111⟩ showing (a) the development of stacking faults from partial dislocation nucleation aligned with (b) the distribution of hydrostatic stress and (c) shear stress in the sample.

⟨111⟩ sample does not exhibit dislocation activity until 1.2 km/s. The ⟨110⟩ sample also exhibits the lowest plastic wave velocity, with the initial plastic wave being measured at approximately 3.7 km/s while the ⟨100⟩, ⟨111⟩, and ⟨123⟩ oriented samples exhibit an initial plastic wave velocity of 5 km/s or greater. Figure 3(a) also shows that the derivative of the plastic wave velocity with respect to the piston velocity changes as the piston velocity increases. This suggests the existence of separate dislocation propagation vs dislocation nucleation regimes that drive the plastic wave. Similar observations for the development of the plastic front for the ⟨110⟩ orientation only were made by Xu *et al.*[30] In addition, the ⟨111⟩ and ⟨123⟩ oriented samples exhibit plastic wave velocity derivatives that are more shallow than ⟨110⟩, suggesting differences in the evolution of the plastic wave for each orientation.

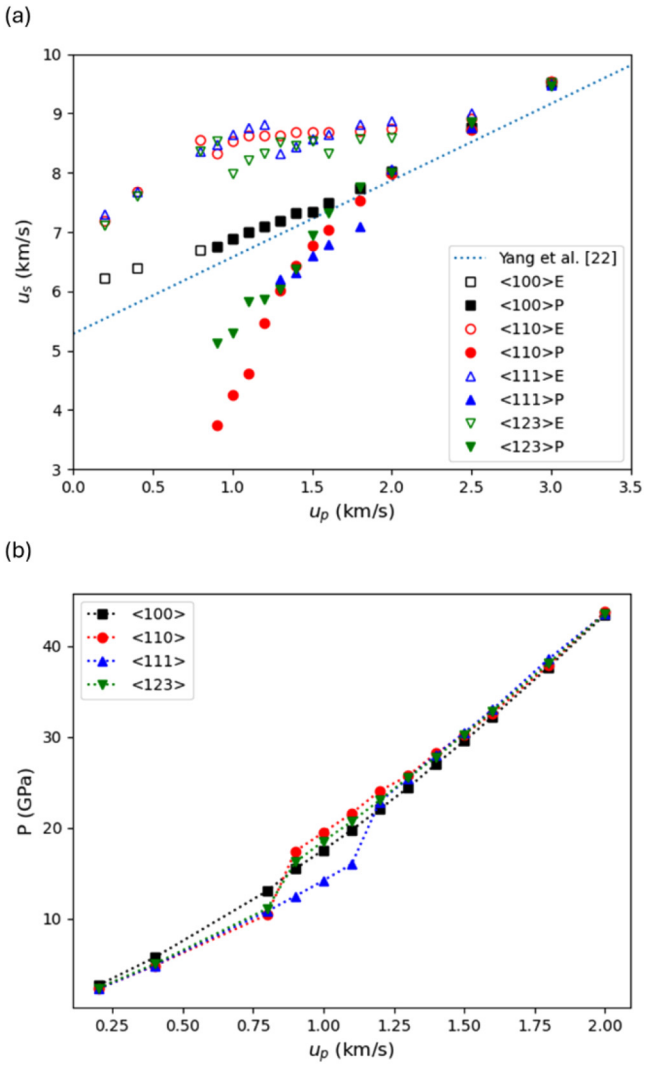

FIG. 3. (a) u_s vs u_p curves and (b) P vs u_p from nonequilibrium MD simulations. The elastic wave velocities are represented with open shapes while the plastic wave velocities are presented as closed shapes in (a). The HEL is identified as the kink in the curve for each orientation in (b).

To elucidate the evolution of stress over all time, x–t diagrams for each shock orientation are presented in Fig. 4. For consistency, the x–t diagrams are presented for a piston velocity 0.1 km/s higher than the HEL for each shock orientation. The hydrostatic stresses in Fig. 4 are normalized in each case by the measured Hugoniot pressure for that sample. An orientation dependence of plastic evolution is clear when comparing the evolution of the stress state over time. For the ⟨100⟩ sample in Fig. 4(a), since there is no elastic–plastic separation, the interface between compressed and uncompressed materials is flat as the wave propagates. However, for ⟨110⟩, ⟨111⟩, and ⟨123⟩ orientations, the separation between the elastic and plastic waves is very clear. Close examination of the ⟨110⟩ sample [Fig. 4(b)] reveals that the interface between the elastic and plastic regions of the compressed material is not flat. Instead, the interface exhibits roughness where streaks in the hydrostatic stress are identified. These streaks are elastodynamic wave emissions associated with the nucleation of dislocations at the plastic wave front and will be further discussed later while analyzing the stress profiles along the length of the sample at a single time step. The ⟨111⟩ shocked sample [Fig. 4(c)] exhibits a large elastic pulse from initial dislocation nucleation that generates an elastodynamic wave. This point in Fig. 4(c) is identified with an arrow and is the first instant at which streaks of white, indicating a drop in hydrostatic stress, is present in the sample. While this occurs for all orientations, it is the most prominent in the ⟨111⟩ direction, where the event creates two cones, a large one in the direction of shock and a smaller one in the opposite direction. When the latter meets the piston interface, it reflects and travels back into the sample. The reflection then travels in the direction of shock seemingly parallel to the elastic wave, indicating that they have nearly the same velocity. This event is similar to the stress fields generated from the injected dislocations described in the context of dislocation dynamics.[41–44] Streaks in the hydrostatic stress originating from the elastic–plastic interface are also present in the ⟨111⟩ oriented sample but are not as regularly spaced as in the ⟨110⟩ oriented sample, which could be due to interference from the large elastodynamic wave that is reflected off the piston. A similar initial pulse of dislocations is seen in the ⟨123⟩ oriented sample [Fig. 4(d)], but the transition between the elastic and plastic regions is slightly more diffuse.

The time after which the regularly spaced elastodynamic wave pulses occur and the plastic wave velocity becomes visually constant is defined as t_{steady}. This point is identified and labeled in Fig. 4 for each of the orientations sampled. After this point, the plastic wave is assumed to be steady and data analysis can be performed without bias from the initial nucleation event in the pristine (dislocation-free) sample. It is significant to note the variation in the amount of time required to reach this point, especially for shock along ⟨111⟩, which requires almost half of the total simulation time. This analysis emphasizes the importance of the selection of model length for shock simulations near the HEL where it takes a significant amount of time for a stable plastic wave to develop.

Stress profiles at $t = 50.0$ ps for $u_p = 1.0$ km/s for ⟨100⟩, ⟨110⟩, and ⟨123⟩ oriented samples and 1.3 km/s for the ⟨111⟩ sample are presented in Fig. 5. This time is selected because it is past t_{steady}

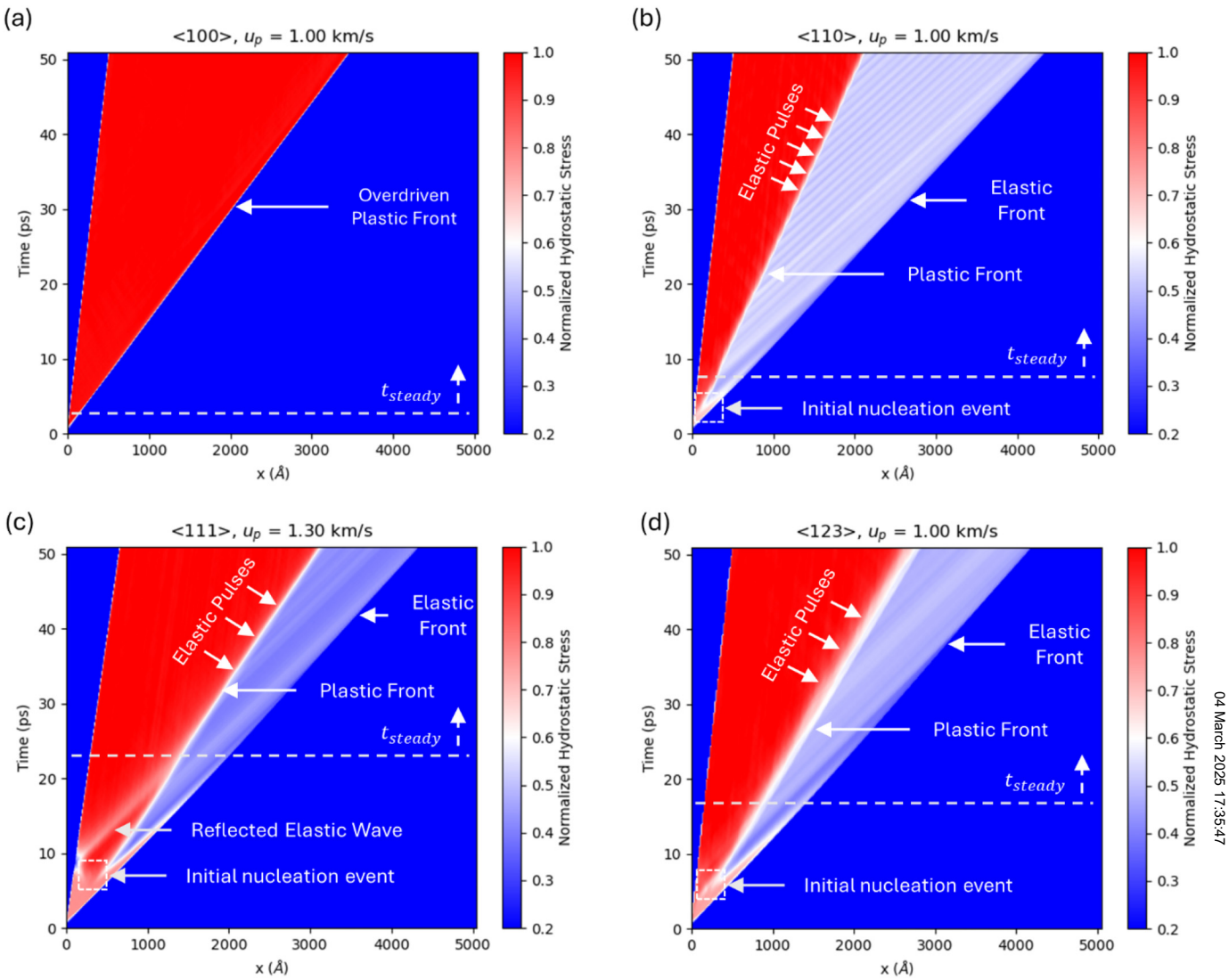

FIG. 4. *x–t* diagrams showing the time and spatial evolution of hydrostatic stress for shock along (a) ⟨100⟩, (b) ⟨110⟩, (c) ⟨111⟩, and (d) ⟨123⟩. The hydrostatic stress is normalized in each case by the measured Hugoniot pressure for that piston velocity. The time of stable plastic wave development is labeled with a dashed line as t_{steady}.

and the plastic wave is considered well developed. Clearly, shock-wave profiles are quite orientation dependent. For the ⟨100⟩ oriented sample in Fig. 5(a), the shear stresses are consistently near zero, characteristic of overdriven shock and continuous dislocation nucleation. In the case of ⟨110⟩ oriented shock, the stresses oscillate between the plastic and elastic fronts due to the dislocation nucleation events, shown initially in Fig. 4. Although not shown for brevity, at higher piston velocities, the magnitude of these oscillations increases along with a decreased elastic–plastic wave separation. The initial stages of these pulses are visible in the profile of $u_p = 1.3$ km/s shock in the ⟨111⟩ sample but are not as regular. The delay for the development of these elastic waves, which travel into the elastic region of the sample, can be traced to the first instance of a homogenous nucleation event that emits a large elastic wave traveling in both directions along the *x* axis. When this wave reflects off the piston, which is defined as a fixed group of atoms that cannot deform, the elastic pulse travels back toward the plastic front. Once it has caught up and becomes coherent with the propagating shockwave, signs of new dislocation nucleation are present that exhibit elastodynamic pulses like those seen in ⟨110⟩⟩. As will be discussed in Sec. IV, this point is important as it gives information as to when the data regarding the onset of plasticity can be obtained at the elastic–plastic interface without any bias from the initial dislocation nucleation event or the piston.

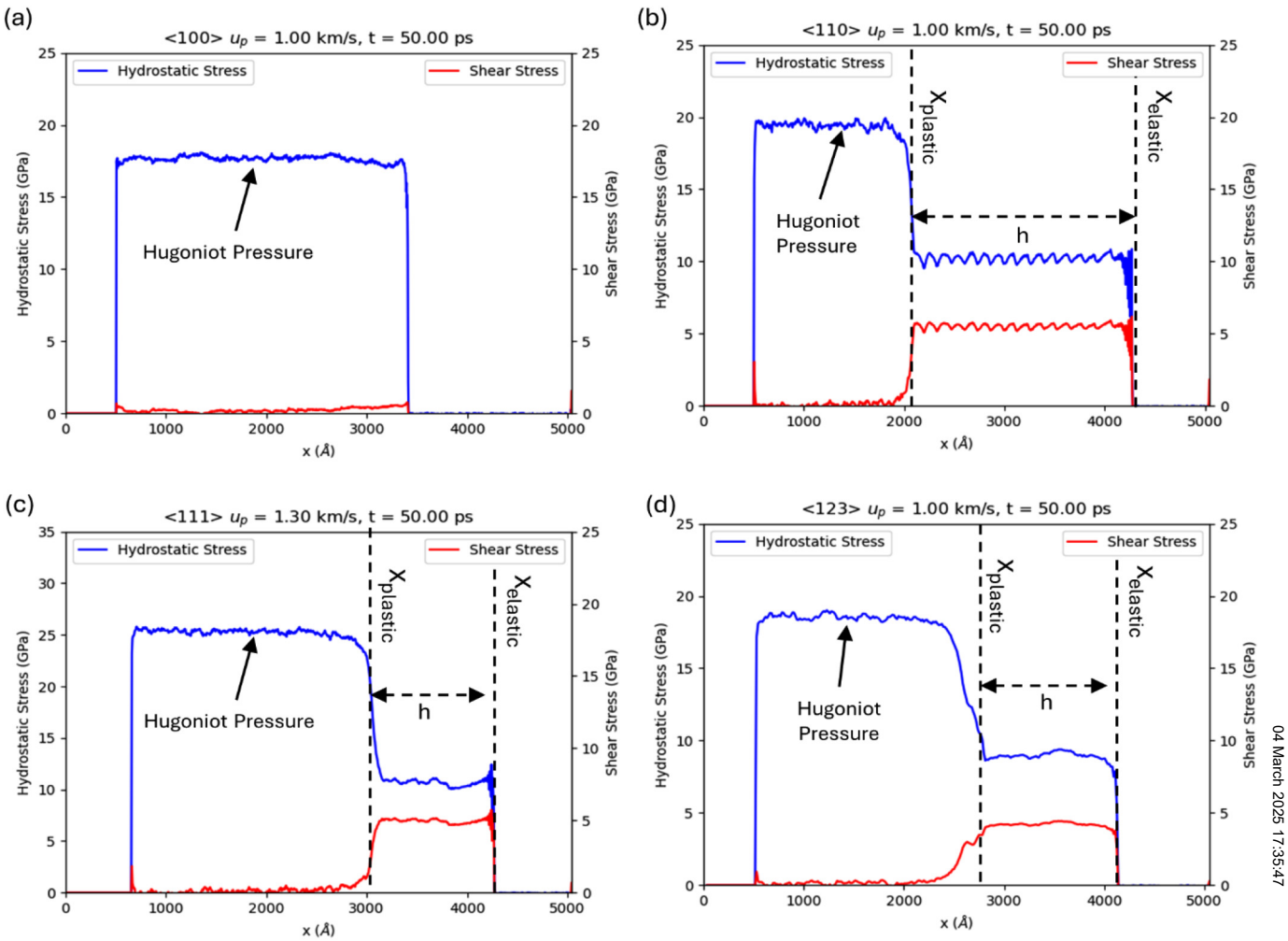

FIG. 5. Hydrostatic and shear stress profiles after 50 ps during shock in (a) ⟨100⟩, (b) ⟨110⟩, (c) ⟨111⟩, and (d) ⟨123⟩.

The x–t diagrams (Fig. 4) presented for the current study have many similarities to those presented by Xu *et al.*, who analyzed shock in the ⟨110⟩ direction, especially the generation of streaks in the elastic region of hydrostatic stress from the points of dislocation nucleation.[30] Furthermore, the shear wave profiles for the ⟨111⟩ sample [Fig. 5(c)] are similar to those presented by Zhakhovsky *et al.* and exhibit the same oscillations in the local stress state that occur at points of dislocation nucleation and multiplication.[31] Overall, these two references demonstrate similar and interrelated phenomena associated with elastic pulses generated by dislocation nucleation and multiplication that is replicated in this study for a variety of shock orientations.

Using stress profiles, the elastic–plastic separation can be determined numerically and measured as the shockwave propagates. In comparing the result of the current MD simulations to the homogenous dislocation nucleation model proposed by Meyers,[6] some key conclusions can be made. First, the Meyers model predicts that as the elastic shock front propagates, dislocations will be periodically nucleated once the deviatoric stresses build up to the point in which dislocation nucleation is required to relax the system strain energy. This would imply a maximum critical distance, h, that the elastic front is allowed to outrun the plastic front until this event occurs and the plastic front instantaneously jumps to catch up with the elastic front. Using the theory presented by Meyers, this distance would be on the order of tens of nanometers,[2,6,24] which is well within the bounds to be captured in the simulation box used in this study. Interestingly, for shock along ⟨110⟩ in this study, the oscillations in elastic wave pulses shown in Figs. 4 and 5 have a period of approximately 14 nm which is in line with the prediction of Meyers. Even though some shock orientations and shock pressures exhibit characteristics that suggest the nucleation of dislocations at regular intervals that drive the plastic wave

forward at a higher rate, the plastic front is never seen to make large jumps in velocity to catch up to the elastic front. In the results from Xu *et al.*,[30] it is discussed that the nucleation of dislocations releases an acoustic wave that relaxes the elastic region to a sub-critical stress state, which decreases the likelihood of nucleation for a short time until the stresses built beyond the HEL again to induce another nucleation. Due to this delay and the inhibition of motion of new dislocations from the pre-existing ones, the elastic wave continuously outpaces the motion of the plastic wave. Zhakhovsky *et al.* concluded that the elastic and plastic waves will eventually reach a synchronized speed where the spacing between them will converge.[31] However, this would require much longer models to confirm as they report elastic–plastic spacings up to 500 nm before converging, which is the length of the sample in this study. Therefore, verification of their conclusion requires longer simulations and further analysis of the phenomena.

IV. LINE DETECTION METHODOLOGY TO MEASURE DISLOCATION SPACING

Quantitative characterization of dislocation spacing during shock loading is performed using a computer vision-based approach, starting with the tools in OVITO.[40] To identify the average spacing of stable dislocation loops in the nucleation zone, a structural definition of the plastic wave position is necessary, to act as a reference point for imaging processes. While the plastic wave position was defined in Sec. III from thermomechanical variables, a structural definition is more useful here to define a moving window centered around new dislocation nucleation activity, as opposed to an average thermomechanical state in the system. Plastic wave position is determined via a one-dimensional binning procedure in which the number of HCP atoms (identified through CNA) is counted and divided by the total number of atoms in each bin. An example of this profile is shown in Fig. 6(a). Using this profile, the plastic front position is identified as the first peak, and at each output step, a thin slice (3 Å) 350 Å behind this point is extracted for analysis. Then, an image is created normal to the direction of shock (the cross section of the sample) using the rendering capabilities in OVITO. In these images, all atoms that exhibit an HCP local structure are colored white with the background colored black. This coloring scheme results in a mostly black image with distinct sets of white lines that correspond to the activated slip systems (stacking faults) that intersect the sample cross section during shock. The slicing and rendering procedures are presented visually in Figs. 6(b) and 6(c).

A probabilistic Hough transform from the OpenCV[45] Python package is used to locate all line segments within the image. The lines are detected by transforming each pixel in the image into Hough space and generating a series of curves based on the algorithm by Matas *et al.*[46] in what is known as the progressive probabilistic Hough transform. Using an approach akin to a Monte Carlo methodology, each pixel in the image is randomly selected and processed in its respective Hough space by converting the Cartesian coordinates (x_i, y_i) to the polar coordinates (ρ, θ). In this transformation, every pixel is then converted to a line in the Hough space. When two lines intersect in Hough space, the two pixels are on the same line defined by (ρ, θ), and if enough intersections are detected for a single line, the algorithm accepts it as a line. A more detailed description of the probabilistic Hough transform algorithm is available in the work of Matas *et al.*[46] as well as the documentation from OpenCV.[45]

The output of this process consists of the endpoints of lines based on the key input parameters,[45] such as the minimum line length, maximum gap between lines, and the threshold for how many pixels must lie on one line in order to be detected as a line. In a traditional Hough transformation, the output would be global lines in space, but the use of the probabilistic Hough transform allows for the detection of individual short line segments. An additional step is implemented that rotates each image, for a particular orientation and piston velocity, to align each set of stacking fault lines that are anticipated from Schmid analysis to the y axis of the image. By adding this step, each set of lines can be detected by only considering the vertically aligned segments, guaranteeing that the line sets are parallel and straight. Using the lines detected, a precise reconstruction of the cross section is created that isolates the stacking faults as straight lines without surrounding noise. Once the stacking fault lines are detected, the spacing between the activated slip systems is characterized using two different methods. In the first method (method 1), the number of lines detected in each image is divided by the cross-sectional area of the sample to obtain an approximation of the dislocation density, ρ. Then, assuming the dislocations are arranged with general uniformity across the representative area, the spacing between dislocations, d, is $\sqrt{\rho^{-1}}$.

In the second method (method 2), the detected lines are converted to a vector based on their direction and partitioned into separate sets of parallel lines that represent each slip system. Since each set of lines is detected as vertical segments, a resulting series of images that consist of a single set of parallel lines for each slip system is obtained. The vertical lines are then collapsed into a one-dimensional array along the x axis where every column of the pixel is identified as having a line or not. Then, these data sets for each slip system in each image are analyzed via a one-dimensional autocorrelation to measure the peak spacing between the detected lines for each slip system. The number of autocorrelations computed for each time step is equal to the number of partitioned line systems. After every image has been analyzed and the average peak spacing is determined from the autocorrelation, the data sets are averaged with each other to calculate an average distance between the activated slip systems for each shock orientation and piston velocity.

An example of stacking fault line detection on a single cross section from the ⟨111⟩ oriented sample is presented in Fig. 7. The detected lines for each activated slip system overlayed on the original image from CNA are presented in Fig. 7(b) where each set of lines is colored as blue, red, or green to illustrate the detection of each slip system orientation independently. In this figure, the lines are given an extra thickness for visualization purposes, but in the method 2 analysis, they are kept at the smallest linewidth possible to avoid peak widening in the computation of the autocorrelations.

Note, for each shock orientation, the procedure outlined is performed on a slice of the shocked model at each time step sampled. Images are collected every 0.5 ps from t_{steady} until 51 ps (where the start of the piston ramp process is 0 ps). The acquisition of data does not begin until t_{steady} to eliminate any effects from piston ramping or the initial elastodynamic wave pulse from the

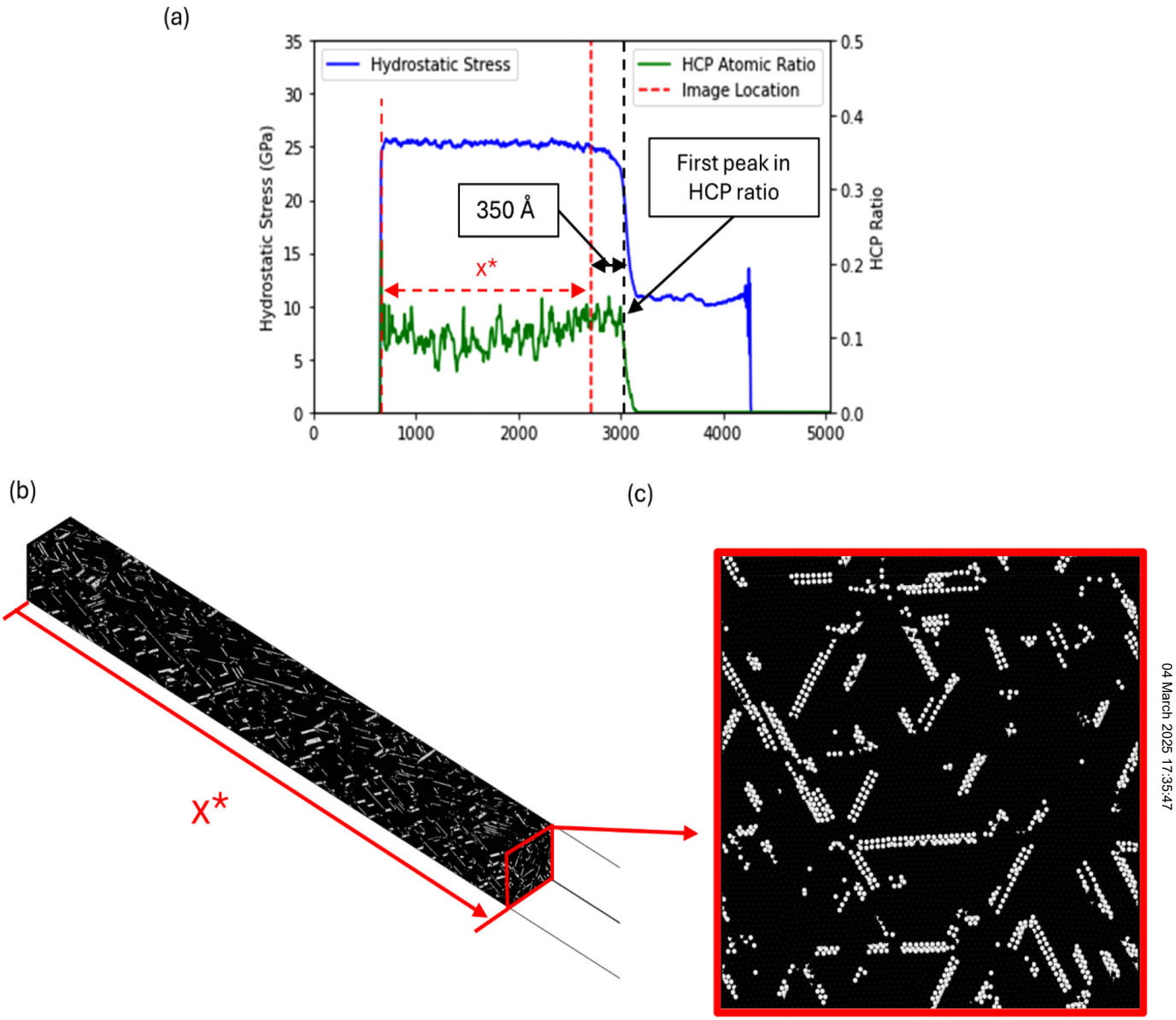

FIG. 6. (a) Procedure to identify the location of the plastic wave and the position of the image, x^*, using the HCP atomic ratio and hydrostatic stress, (b) sliced image of a shocked MD simulation cell at position x^*, and (c) the resulting image showing stacking faults intersecting the cross section.

first dislocation nucleation event, as discussed in Sec. III. The x–t diagram for the ⟨111⟩ oriented sample at $u_p = 1.3$ km/s presented in Fig. 4(c) suggests the significance of this value, since after this point, elastodynamic wave pulses coming from the elastic–plastic interface become much more frequent as indicated by the white streaks emanating from the interface between the two regions. Prior to this time, the elastic pulses do not exhibit what can be interpreted as periodic behavior. The beginning stages of these oscillations can be seen in Fig. 5(c) for the stress profile of the ⟨111⟩ sample where the oscillations trail a mostly flat region just behind the elastic front. The exact nature and mechanics of these oscillations are not clear and the time-dependence of their development relative to the initial nucleation are beyond the scope of this paper. Thus, data are only collected after this point as the wave is considered to be fully developed with the stable nucleation patterns present.

A primary advantage of the probabilistic Hough transformation is that it can recognize and combine lines that are segmented

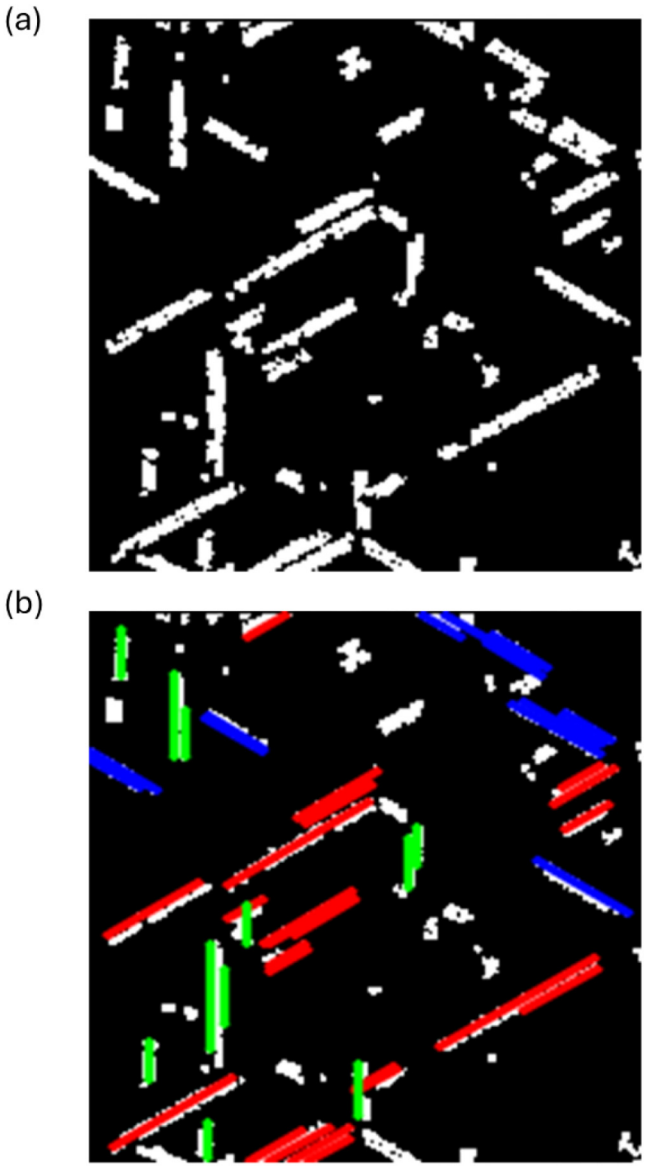

FIG. 7. (a) Stacking faults identified using CNA that intersect an example cross section of the shocked ⟨111⟩ oriented sample with $u_p = 1.3$ km/s and (b) the detected lines colored blue, red, and green for each set of slip planes detected in the image.

slightly from one another due to the limitations of CNA to identify structures at junctions and in regions with very high thermal fluctuations. Other methodologies to characterize dislocation activity, such as the dislocation extraction algorithm (DXA)[47] and clustering the HCP atoms based on the results of CNA, may do a poor job in characterizing heavily disordered regions. For example, clustering based on a local structure may create groups that are too large, combining stacking faults that cross one another, or many

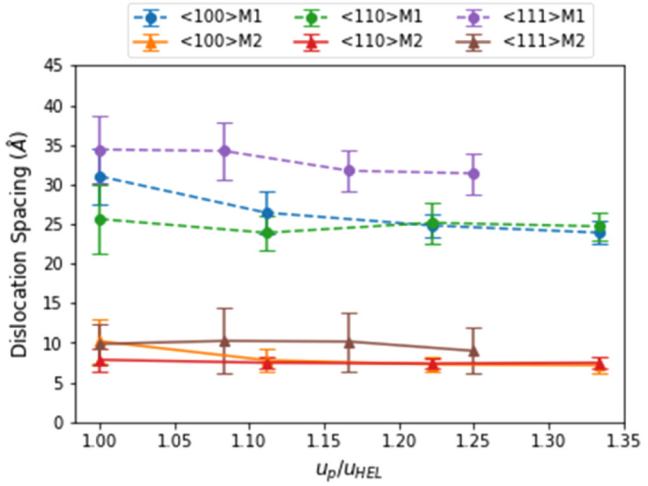

FIG. 8. Dislocation spacing measurements from method 1 (dashed lines with circles) and method 2 (solid lines with triangles) with associated error bars as the standard deviation of the data set.

disconnected groups that visually should be identified as a single stacking fault. The hyperparameters associated with the methodology developed here allow for gaps between line segments and define thresholds for what should be identified as a line or stacking fault, enabling the combination of segmented lines that are likely to be of the same object in reality.

For each sample and piston velocity, there are approximately 40–62 measurements of spacing between the detected stacking faults obtained that are averaged and allow a measurement of standard deviation for each data set. If an image is identified to have no lines present, because it was taken in a region that was too disordered to correctly identify the stacking faults, it is disregarded. Additionally, this analysis is only performed on the ⟨100⟩, ⟨110⟩, and ⟨111⟩ oriented shocked samples as the ⟨123⟩ oriented sample displays a more complex development of dislocation behavior with respect to the preference of the activated slip systems. In this orientation, Schmid analysis identifies the maximum Schmid factor of a single slip plane to be 0.4666, but there exists another plane with a Schmid factor of 0.3499. This secondary slip system is close enough to the maximum that it does appear in the shocked sample, but with a lower likelihood for a given shock pressure. This means the different slip systems would vary in their respective frequencies of detection and spacing. Since the methodology developed in this study assumes each slip system or set of lines to be equally likely, this orientation is omitted from the analysis.

V. DISLOCATION SPACING RESULTS AND DISCUSSION

The results of method 1 and method 2 are displayed in Fig. 8 with error bars from the standard deviation across all images analyzed from each sample. In this plot, the x axis is normalized with respect to the HEL for each orientation where plasticity first occurs, since the ⟨111⟩ oriented sample exhibits a higher HEL than the

⟨100⟩ and ⟨110⟩ oriented samples. These results reveal that as the shock pressure increases, the average dislocation spacing modestly decreases for the ⟨100⟩ and ⟨111⟩ orientations when using method 1. The ⟨110⟩ oriented samples do not demonstrate the same shock pressure dependence on dislocation spacing. Using method 2, the same conclusions cannot be made regarding a decrease in dislocation spacing with increasing piston velocity. The spacing between the activated dislocations is essentially constant as the piston velocity increases and the spacing between the activated slip systems is not orientation dependent either, as is observed from the results of method 1. For validation of the sample dimensions, a series of simulations were performed on the ⟨111⟩ oriented samples with lateral dimensions of $40 \times 40\ \text{nm}^2$ with no significant difference in the results found. However, while there were no significant differences detected and the lateral dimensions are similar to those used in the literature,[21,35] there is a possibility of size dependence at even larger lateral dimensions.

The differences between the method 1 and 2 results presented in Fig. 8 are due to several factors. First, the two methods are measuring two different, but related, quantities. Method 1 is focused on all dislocations that intersect each snapshot during shock loading and measures spacing considering the total number detected among all activated slip systems, regardless of the slip systems activated. The spacing within the cross section is assumed to be uniform for all lines. For method 2, the spacing is a more direct measurement between each set of parallel activated slip planes. Therefore, each set of lines detected only has a measurement associated with dislocations on the same slip system, offering information on the average spacing between similar types of dislocation activities but less on the state of the entire system. There could be a case in which there are very few dislocations in the system, but method 2 would present a small spacing if these dislocations are clustered in a small region of the image.

In either case, the spacing between nucleated dislocations measured in this study are significantly smaller than the values predicted by Meyers,[9] which are on the order of 10–20 nm as opposed to the 1–3 nm range obtained using the MD simulations. The model proposed by Meyers is a two-dimensional idealization of a complex three-dimensional problem and lacks the influence of temperature on nucleation kinetics.[41,48,49] While they did not study the same material, Jarmakani *et al.*[2] and Cao *et al.*[50] presented data on the spacing between stacking faults generated for FCC Cu that are between 1 and 12 nm, although their methods for computing this spacing is not explicitly described. While these results cannot be compared one-to-one, they offer some insight into the scale that could be expected. Furthermore, the effects of pre-existing dislocations and various regimes of dislocation nucleation activity have been discussed in the work of Xu *et al.*[30] The effects of these regimes on the spacing between new dislocations and their associated multiplication to form stacking faults should be explored further to determine the interlinking between shock pressure and dislocation–dislocation interactions as nucleation occurs.

It is also important to note that there is an orientation dependence to the accuracy of the line detection since the stacking fault lines detected are a projection onto the plane that the image is taken, resulting in the variation of thickness of the lines dependent on the orientation of the respective slip systems to the direction of shock. Stacking faults that are very thick may be large enough to be detected as multiple lines that are closer together even if they are one activated slip plane. A more intelligent line merging algorithm that ensures only one line is detected per stacking fault would aid in decreasing this error. Currently, merging is based on the distance the endpoints of the lines are from one another, which serves well to decrease lines that overlay one another, but may miss those that are on the same stacking fault line but are offset from each other.

A final limitation of both methods is the accuracy of CNA on the highly compressed state of Al during shock compression. To accurately detect the presence of stacking faults, CNA must be able to detect HCP atoms in large enough clusters that show up as lines in images. In the compressed region behind the shock front, much of the material may be identified as a BCC structure (depending on the compression axis) or as "other" to indicate it is too disordered to have a structure labeled. Both structures are a result of the CNA algorithm misinterpreting the compressed atoms and this worsens as the shock pressure increases. Furthermore, as the stacking fault density is expected to increase with the rise of shock pressure, the number of dislocation junctions increases, which creates disordered regions that are difficult for the CNA algorithm to cleanly detect. This results in a lower proportion of acceptable lines to be detected by the probabilistic Hough transform even though there is more plastic deformation present, limiting the range of piston velocities that are capable of being sampled by the current methodology.

VI. CONCLUSIONS

Molecular dynamics simulations are performed to study the shock of single-crystal Al oriented along ⟨100⟩, ⟨110⟩, ⟨111⟩, and ⟨123⟩ to study the spatial relationship between dislocations in the nucleation zone behind the plastic wave front. Spatial binning of hydrostatic and shear stresses indicates that plasticity during shock is orientation dependent, specifically, the elastic–plastic spacing and the derivative of the plastic wave velocity with respect to the piston velocity. Oscillations in hydrostatic stress in the elastic region, shown in both x–t diagrams and stress profiles at an individual snapshot in time, offer evidence of dislocation nucleation at regular intervals and the elastodynamic stress pulses that travel into the elastically compressed region.

In what is to the authors knowledge, the first quantitative approach to this problem, samples oriented along ⟨100⟩, ⟨110⟩, and ⟨111⟩ are analyzed using a computer-vision based algorithm leveraging the development of stacking fault lines detected with common-neighbor analysis to quantify the spacing between nucleated dislocations. Measuring the spacing between stacking faults by calculating the density of detected lines in a series of images for each crystal orientation (method 1), an orientation dependence of dislocation spacing is found in addition to a modest decrease in spacing as the shock pressure increases. When the spacing between each set of lines is computed using an autocorrelation of each set of parallel lines (method 2), the results yield no such dependence on shock pressure or orientation.

The methodology presented to obtain the measurements of dislocation spacing is not unique to Al and can be applied to other FCC metals with appropriate tuning of computer-vision parameters. In fact, it may be more accurate for FCC materials with low

stacking fault energy because of the naturally wider separation between Shockley partial dislocations than in Al. Additionally, the analysis is not limited to shock loading and can be applied to any loading state in which the spatial characterization of dislocation activity is sought to be obtained.

ACKNOWLEDGMENTS

The authors acknowledge the support provided by National Nuclear Security Administration (NNSA) under Contract No. DE-NA0004088 and the University of Florida. The authors acknowledge University of Florida Research Computing for providing computational resources and support that have contributed to the research results reported in this publication.

AUTHOR DECLARATIONS

Conflict of Interest

The authors have no conflicts to disclose.

Author Contributions

Andre Archer: Conceptualization (equal); Data curation (lead); Formal analysis (lead); Methodology (equal); Validation (lead); Visualization (lead); Writing – original draft (lead); Writing – review & editing (supporting). **Kaitlyn Campbell:** Formal analysis (supporting); Methodology (supporting); Validation (supporting); Visualization (supporting). **Douglas E. Spearot:** Conceptualization (equal); Funding acquisition (lead); Methodology (equal); Project administration (lead); Resources (lead); Supervision (lead); Writing – review & editing (equal).

DATA AVAILABILITY

The Python code to compute the data presented will be available at the corresponding author's GitHub.

REFERENCES

[1]F. Coppari, T. de Rességuier, S. Razorenov, T. Sekine, and E. Zaretsky, "Shock behavior of materials," J. Appl. Phys. **133**(5), 050401 (2023).
[2]H. N. Jarmakani, E. M. Bringa, P. Erhart, B. A. Remington, Y. M. Wang, N. Q. Vo, and M. A. Meyers, "Molecular dynamics simulations of shock compression of nickel: From monocrystals to nanocrystals," Acta Mater. **56**(19), 5584–5604 (2008).
[3]D. Choudhuri and Y. M. Gupta, "Shock compression of aluminum single crystals to 70 GPa: Role of crystalline anisotropy," J. Appl. Phys. **114**(15), 153504 (2013).
[4]D. Choudhuri and Y. M. Gupta, AIP Conf. Proc. **1426**(1), 755–758 (2012).
[5]P. M. Anderson, J. P. Hirth, and J. Lothe, *Theory of Dislocations* (Cambridge University Press, 2017).
[6]M. A. Meyers, H. Jarmakani, E. M. Bringa, and B. A. Remington, "Chapter 89 dislocations in shock compression and release," in *Dislocations Solids* (Elsevier, 2009), pp. 91–197.
[7]C. S. Smith, "Metallographic studies of metals after explosive shock," Trans. Metall. Soc. AIME **212**, 574–589 (1958).
[8]E. Hornbogen, "Shock-induced dislocations," Acta Metall. **10**(10), 978–980 (1962).
[9]M. A. Meyers, F. Gregori, B. K. Kad, M. S. Schneider, D. H. Kalantar, B. A. Remington, G. Ravichandran, T. Boehly, and J. S. Wark, "Laser-induced shock compression of monocrystalline copper: Characterization and analysis," Acta Mater. **51**(5), 1211–1228 (2003).
[10]M. A. Meyers, "A mechanism for dislocation generation in shock-wave deformation," Scr. Metall. **12**(1), 21–26 (1978).
[11]J. Weertman, "Moving dislocations in a shock front," in *Shock Waves and High-Strain-Rate Phenomena in Metals: Concepts and Applications*, edited by M. A. Meyers and L. E. Murr (Springer US, Boston, MA, 1981), pp. 469–486.
[12]J. Weertman and P. S. Follansbee, "Dislocation dynamics and plastic shock waves," Mech. Mater. **7**(3), 177–189 (1988).
[13]Y.-P. Pellegrini and M. Josien, "Shock-driven nucleation and self-organization of dislocations in the dynamical Peierls model," Phys. Rev. B **108**(5), 054309 (2023).
[14]M. A. Mogilevsky and P. E. Newman, "Mechanisms of deformation under shock loading," Phys. Rep. **97**(6), 357–393 (1983).
[15]B. L. Holian, "Modeling shock-wave deformation via molecular dynamics," Phys. Rev. A **37**(7), 2562–2568 (1988).
[16]N. K. Bourne, J. C. F. Millett, M. Chen, J. W. McCauley, and D. P. Dandekar, "On the Hugoniot elastic limit in polycrystalline alumina," J. Appl. Phys. **102**(7), 073514 (2007).
[17]L. He, F. Wang, X. Zeng, X. Yang, and Z. Qi, "Atomic insights into shock-induced spallation of single-crystal aluminum through molecular dynamics modeling," Mech. Mater. **143**, 103343 (2020).
[18]Y. Ju, Q. Zhang, Z. Gong, G. Ji, and L. Zhou, "Molecular dynamics simulation of shock melting of aluminum single crystal," J. Appl. Phys. **114**(9), 093507 (2013).
[19]Y. Liao, M. Xiang, X. Zeng, and J. Chen, "Molecular dynamics studies of the roles of microstructure and thermal effects in spallation of aluminum," Mech. Mater. **84**, 12–27 (2015).
[20]S. V. Razorenov, AIP Conf. Proc. **620**, 503–506 (2002).
[21]A. Sharma and D. K. Dubey, "Effect of porosity on shock propagation behaviour of single crystal aluminium: A molecular dynamics investigation," Mech. Mater. **177**, 104535 (2023).
[22]X. Yang, X. Zeng, C. Pu, W. Chen, H. Chen, and F. Wang, "Molecular dynamics modeling of the Hugoniot states of aluminum," AIP Adv. **8**(10), 105212 (2018).
[23]J. A. Zimmerman, J. M. Winey, and Y. M. Gupta, "Elastic anisotropy of shocked aluminum single crystals: Use of molecular dynamics simulations," Phys. Rev. B **83**(18), 184113 (2011).
[24]E. M. Bringa, J. U. Cazamias, P. Erhart, J. Stölken, N. Tanushev, B. D. Wirth, R. E. Rudd, and M. J. Caturla, "Atomistic shock Hugoniot simulation of single-crystal copper," J. Appl. Phys. **96**(7), 3793–3799 (2004).
[25]I. A. Bryukhanov, "Atomistic simulation of the shock wave in copper single crystals with pre-existing dislocation network," Int. J. Plast. **151**, 103171 (2022).
[26]B. L. Holian and P. S. Lomdahl, "Plasticity induced by shock waves in nonequilibrium molecular-dynamics simulations," Science **280**(5372), 2085–2088 (1998).
[27]M. M. Sichani and D. E. Spearot, "A molecular dynamics study of dislocation density generation and plastic relaxation during shock of single crystal Cu," J. Appl. Phys. **120**(4), 045902 (2016).
[28]R. Valisetty, A. Rajendran, G. Agarwal, A. Dongare, J. Ianni, and R. Namburu, "HPC simulations of shock front evolution for a study of the shock precursor decay in a submicron thick nanocrystalline aluminum," Model. Simul. Mater. Sci. Eng. **26**(5), 055008 (2018).
[29]S. Zhao, Z. Li, C. Zhu, W. Yang, Z. Zhang, D. E. J. Armstrong, P. S. Grant, R. O. Ritchie, and M. A. Meyers, "Amorphization in extreme deformation of the CrMnFeCoNi high-entropy alloy," Sci. Adv. **7**(5), eabb3108 (2021).
[30]Y. F. Xu, S. C. Hu, Y. Cai, and S. N. Luo, "Origins of plastic shock waves in single-crystal Cu," J. Appl. Phys. **131**(11), 115901 (2022).
[31]V. V. Zhakhovsky, M. M. Budzevich, N. A. Inogamov, I. I. Oleynik, and C. T. White, "Two-zone elastic-plastic single shock waves in solids," Phys. Rev. Lett. **107**(13), 135502 (2011).
[32]A. P. Thompson, H. M. Aktulga, R. Berger, D. S. Bolintineanu, W. M. Brown, P. S. Crozier, P. J. in 't Veld, A. Kohlmeyer, S. G. Moore, T. D. Nguyen, R. Shan,

M. J. Stevens, J. Tranchida, C. Trott, and S. J. Plimpton, "LAMMPS—A flexible simulation tool for particle-based materials modeling at the atomic, meso, and continuum scales," Comput. Phys. Commun. **271**, 108171 (2022).
[33]V. V. Zhakhovskii, N. A. Inogamov, Y. V. Petrov, S. I. Ashitkov, and K. Nishihara, "Molecular dynamics simulation of femtosecond ablation and spallation with different interatomic potentials," Appl. Surf. Sci. **255**(24), 9592–9596 (2009).
[34]Y. Mishin, D. Farkas, M. J. Mehl, and D. A. Papaconstantopoulos, "Interatomic potentials for monoatomic metals from experimental data and *ab initio* calculations," Phys. Rev. B **59**(5), 3393–3407 (1999).
[35]T. C. Germann, B. L. Holian, P. S. Lomdahl, and R. Ravelo, "Orientation dependence in molecular dynamics simulations of shocked single crystals," Phys. Rev. Lett. **84**(23), 5351–5354 (2000).
[36]P. Wen, G. Tao, D. E. Spearot, and S. R. Phillpot, "Molecular dynamics simulation of the shock response of materials: A tutorial," J. Appl. Phys. **131**(5), 051101 (2022).
[37]D. Faken and H. Jónsson, "Systematic analysis of local atomic structure combined with 3D computer graphics," Comput. Mater. Sci. **2**(2), 279–286 (1994).
[38]H. Tsuzuki, P. S. Branicio, and J. P. Rino, "Structural characterization of deformed crystals by analysis of common atomic neighborhood," Comput. Phys. Commun. **177**(6), 518–523 (2007).
[39]C. L. Kelchner, S. J. Plimpton, and J. C. Hamilton, "Dislocation nucleation and defect structure during surface indentation," Phys. Rev. B **58**(17), 11085–11088 (1998).
[40]A. Stukowski, "Visualization and analysis of atomistic simulation data with OVITO—The open visualization tool," Model. Simul. Mater. Sci. Eng. **18**(1), 015012 (2009).
[41]M. A. Shehadeh and H. M. Zbib, "On the homogeneous nucleation and propagation of dislocations under shock compression," Philos. Mag. **96**(26), 2752–2778 (2016).
[42]B. Gurrutxaga-Lerma, D. S. Balint, D. Dini, D. E. Eakins, and A. P. Sutton, "Attenuation of the dynamic yield point of shocked aluminum using elastodynamic simulations of dislocation dynamics," Phys. Rev. Lett. **114**(17), 174301 (2015).
[43]B. Gurrutxaga-Lerma, D. S. Balint, D. Dini, D. E. Eakins, and A. P. Sutton, "A dynamic discrete dislocation plasticity method for the simulation of plastic relaxation under shock loading," Proc. R. Soc. Math. Phys. Eng. Sci. **469**(2156), 20130141 (2013).
[44]N. Bertin, M. Upadhyay, C. Pradalier, and L. Capolungo, "A FFT-based formulation for efficient mechanical fields computation in isotropic and anisotropic periodic discrete dislocation dynamics," Model. Simul. Mater. Sci. Eng. **23**, 065009 (2015).
[45]"OpenCV: Feature detection," Open Source Computer Vision Database; available at https://docs.opencv.org/3.4/dd/d1a/group__imgproc__feature.html#ga8618180a5948286384e3b7ca02f6feeb.
[46]J. Matas, C. Galambos, and J. Kittler, "Robust detection of lines using the progressive probabilistic Hough transform," Comput. Vision Image Understanding **78**(1), 119–137 (2000).
[47]A. Stukowski and K. Albe, "Extracting dislocations and non-dislocation crystal defects from atomistic simulation data," Model. Simul. Mater. Sci. Eng. **18**(8), 085001 (2010).
[48]M. A. Shehadeh, E. M. Bringa, H. M. Zbib, J. M. McNaney, and B. A. Remington, "Simulation of shock-induced plasticity including homogeneous and heterogeneous dislocation nucleations," Appl. Phys. Lett. **89**(17), 171918 (2006).
[49]Y. Cui, G. Po, Y.-P. Pellegrini, M. Lazar, and N. M. Ghoniem, "Computational 3-dimensional dislocation elastodynamics," J. Mech. Phys. Solids **126**, 20–51 (2019).
[50]B. Cao, E. M. Bringa, and M. A. Meyers, "Shock compression of monocrystalline copper: Atomistic simulations," Metall. Mater. Trans. A **38**(11), 2681–2688 (2007).